Feedback mechanisms between precipitation and dissolution reactions across randomly heterogeneous conductivity fields

Yaniv Edery[1], Martin Stolar[1], Giovanni Porta[2], Alberto Guadagnini[2]

[1] Faculty of Civil and Environmental Engineering, Technion, Haifa, Israel

[2]Department of Civil and Environmental Engineering, Politecnico di Milano, 20133, Milan, Italy;

Corresponding author: Yaniv Edery

Highlights

- Regions of prevailing precipitation and dissolution are related to preferential flow patterns
- Large changes in non-Fickian transport parameters are observed while velocity variance display modest variations
- Initial heterogeneity facilitates attaining asymptotic average solute velocity value

Abstract

Our study investigates interplays between dissolution, precipitation, and transport processes taking place across randomly heterogeneous conductivity domains and the ensuing spatial distribution of preferential pathways. We do so by relying on a collection of computational analyses of reactive transport performed in two-dimensional systems where the (natural) logarithm of conductivity is characterized by various degrees of spatial heterogeneity. Our results document that precipitation and dissolution jointly take place in the system, the latter mainly occurring along preferential flowpaths associated with the conductivity field, the former being observed at locations close to and clearly separated from these. High conductivity values associated with the preferential flowpaths tend to further increase in time, giving rise to a self-sustained feedback between transport and reaction processes. The clear separation between regions where dissolution or precipitation takes place is imprinted onto the sample distributions of conductivity which tend to become visibly left skewed with time (with the appearance of a bimodal behavior at some times). The link between conductivity changes and reaction-driven processes promotes the emergence of non-Fickian effective transport features. The latter can be captured through a continuous time random walk model where solute travel times are approximated with a truncated power law probability distribution. The parameters of such a model shift towards values associated with increasingly high non-Fickian effective transport behavior as time progresses.

1.Introduction

Diagnosis and characterization of the feedback between geochemical precipitation/dissolution reactions and solute transport processes in heterogeneous subsurface systems is key to a variety of environmental and Earth science scenarios (Rege & Fogler, 1989; Berkowitz et al., 2016). A critical challenge is the emergence of complex dependencies between physical and chemical processes taking place across aquifer bodies (Saripalli et al., 2001). Heterogeneity of these systems promotes diverse patterns of precipitation and/or dissolution that may imprint a variety of dynamic system responses, including, e.g., wormholing and oscillatory behaviors of system attributes such as porosity and

1

permeability (Edery et al., 2011; Garing et al., 2015; Golfier et al., 2002). Examples of practical applications in this context include geologic CO_2 storage (e.g., Pawar et al., 2015; Noiriel & Daval, 2017; Cabeza et al., 2020 and references therein), acid injection in production wells (e.g., Liu et al., 2017 and references therein), and reactive transport of contaminants (e.g., Ceriotti et al., 2018; Dalla Libera et al., 2020 and references therein).

Computational studies can assist the analysis of patterns of chemical transport across heterogeneous subsurface systems in the presence of precipitation/dissolution phenomena. While requiring an explicit description of the spatial heterogeneity of the system properties (Atchley et al., 2014), routine application of numerical simulations in practical settings is hampered by (*i*) our limited knowledge of the system attributes, resulting in uncertainty affecting the parameterization of the underlying physical and chemical processes and their variability, and (*ii*) the computational costs required to properly quantify such uncertainties and their propagation onto environmental quantities of interest. In this context, we rely on an effective approach to characterize the evolution of key features of solute transport in the presence of rock-fluid interactions across a porous medium whose spatially heterogeneous conductivity field is interpreted according to a commonly employed stochastic framework.

A critical element we tackle is related to the analysis of the dynamic feedback between reactive transport and spatially heterogenous distributions of porous media attributes such as hydraulic conductivity. Following prior studies, we start by recognizing that, even under geochemical equilibrium conditions, the spatial heterogeneity of system attributes typically imprints an uneven spatial distribution of regions where chemical reactions take place, local fluctations of conductivity being key to this element (Edery, Porta, et al., 2016). Further to this, our conceptualization of the setting is grounded on the observation that rendering of transport features in geological formations through effective formulations typically requires embedding non-Fickian features. To this end, we rely on an upscaled description of transport where solute travel/waiting times are approximated with a truncated power law probability density function (PDF), hereafter termed TPL (Berkowitz et al., 2006). This effective description is particularly relevant because the emergence of non-Fickian transport features in heterogeneous formations has been observed at diverse scales of observation, including pore-, laboratory- and field-scale scenarios (e.g., Edery et al., 2011; Muljadi et al., 2018; Menke et al., 2018 and references therein).

In line with our objective, we rest on the framework of analysis developed in (Edery et al., 2014; Edery, Porta, et al., 2016), where an effective depiction of transport processes is parametrized as a function of the statistics of solute residence times in randomly heterogeneous conductivity fields. A main element of this framework is that it yields a link between the TPL weighting times and the occurrence of preferential pathways that can be obtained from computational studies of transport in such conductivity fields (Edery et al., 2014). As a result, the methodology is conducive to an effective (or upscaled) representation of local features to identify signatures of non-Fickian transport (see also, e.g., Dentz et al., 2011; Edery et al., 2014). To illustrate the main features associated with the scenario of interest, we consider a Darcy-scale formulation of a reactive transport setup, where precipitation and/or dissolution of minerals are driven by the injection of an acid compound establishing local equilibrium with the resident fluid and a solid matrix of the host porous medium which is considered to be composed of calcite mineral. While the geochemical processes we consider are somehow streamlined with respect to a field-scale scenario (see, e.g., Lichtner, 1988; Dreybrodt et al., 1996), they embed the main elements characterizing the interplay between solute transport and rock-fluid interactions in Darcy-scale systems (e.g., Edery et al., 2011). Within this conceptual picture, our study aims at investigating (*i*) the interplay between the reactive process and the ensuing spatial distribution

88 of preferential pathways associated with spatially heterogeneous conductivities and (*ii*) the link
89 between locally occurring reaction-driven phenomena and emerging non-Fickian effective transport
90 features, as captured by the TPL formulation of the PDF of particle travel/waiting times.

<div align="center">

2.Methodology

2.1 Chemical model

</div>

93 We simulate a reactive transport scenario where calcite ($CaCO_{3\,(s)}$, subscript (*s*) denoting solid
94 mineral) can dissolve or precipitate locally in the presence of chemical equilibrium between dissolved
95 carbonic acid (H_2CO_3) and pH. The amount of dissolved H_2CO_3 as a function of pH (see Figure S1
96 in the supplementary material) is then governed by equilibrium conditions, which is tantamount to
97 assuming a locally instantaneous reaction (i.e., as the reactive time scale approaches zero at
98 equilibrium, this scenario corresponds to a local Damköhler number which tends to infinity). The
99 formulation describing the chemical reactions can then be streamlined as:

100 $$CaCO_{3\,(s)} \leftrightarrow Ca^{2+} + CO_3^{2-} \tag{1a}$$

101 $$H_2CO_3 \leftrightarrow 2H^+ + CO_3^{2-} \tag{1b}$$

102 according to which two protons H^+ in (1b) react with CO_3^{2-} to produce H_2CO_3 that in turn drives
103 dissolution of the host calcium carbonate solid matrix. While simplified (see, e.g., Lichtner, 1988;
104 Dreybrodt et al., 1996), the chemical set-up follows previous work by Edery et al. (2011), where there
105 is an extensive assessment of the employed formulation (see also the Supplementary Material). In
106 this context, and consistent with typical experimental practice, we consider the injected fluid and the
107 porous medium to be associated with a source of H^+ and an abundance of Ca^{2+}, respectively. Thus,
108 Ca^{2+} is not rate limiting and the spatial distribution of H^+, as driven by transport and reaction,
109 governs pH. The rate limiting reaction is then (1b), that is controlled by the available H^+ (or pH),
110 similar to observations associated with other studies (Singurindy & Berkowitz, 2004; Edery et al.,
111 2011). The chemical reaction system (1a) and (1b) is here simplified (see, e.g., Krauskopf & Bird,
112 1967) through:

113 $$co \leftrightarrow 2h + c \tag{2}$$

114 where co denotes H_2CO_3, h and c representing H^+ and $CaCO_{3\,(s)}$, respectively.

<div align="center">

2.2 Flow and transport modeling

</div>

116 Our computational setting is intended to mimic a laboratory scale scenario where a 60×24 cm^2
117 two-dimensional flow cell is filled with a porous system formed by a $CaCO_{3\,(s)}$ solid matrix. The
118 system is initially fully saturated with water and an injection of low pH water takes place across the
119 upstream side of the cell. To investigate the influence of the dissolution/precipitation reaction on
120 solute transport, we consider a uniform in the mean groundwater flow, taking place within a two-
121 dimensional domain where the (natural) logarithm of conductivity, $y = \ln(k)$, is considered as a
122 zero-mean, second-order stationary random field. The latter is further characterized by an isotropic,
123 simple exponential, covariance function, with (normalized) correlation length *l/L*, *L* being the length
124 of the domain along the main flow direction. Various degrees of heterogeneity of the system are
125 analyzed upon considering values of log-conductivity variance $\sigma_0^2 = [1, 3, 5]$, subscript 0 denoting
126 that these values refer to the initially generated conductivity distributions (i.e., prior to the occurrence
127 of reactions). The domain is discretized through 300×120 elements of uniform size $\Delta = 0.2$ cm,

128   yielding a field size of 60×24 cm^2. Each field is synthetically generated through the widely tested
129   sequential Gaussian simulator GCOSIM3D (Gómez-Hernández & Journel, 1993) and is characterized
130   by $l/L = 0.016$. This yields a value of $\Delta/l = 0.2$, which is deemed adequate to capture the local features
131   of the covariance of y and their impact on the main statistics of the velocity field and travel times
132   (Ababou et al., 1989; Riva et al., 2009). We note that, while our study is representative of a laboratory
133   scale analysis, the dimensions of the domain have no particular implication and they are only selected
134   to ensure a meaningful description of the correlation structure that is included in the initially generated
135   conductivity fields.

136   For each value of σ_0^2, 20 random realizations of y are generated, each being then subject to a
137   deterministic pressure drop ($\Delta H = 100$cm) between the inlet (left) and the outlet (right) sides. The
138   local distribution of fluid velocity is computed through

139    $$\nabla \cdot \boldsymbol{q}(\boldsymbol{x}) = 0; \boldsymbol{q}(\boldsymbol{x}) = -k(\boldsymbol{x}) \cdot \nabla h(\boldsymbol{x}) \tag{3}$$

140   where $\boldsymbol{q}(\boldsymbol{x})$ is the local Darcy flux, vector $\boldsymbol{x}$ corresponding to spatial location. The local fluid velocity
141   field is then obtained as $\boldsymbol{v} = \boldsymbol{q}/\theta$, a constant initial porosity $\theta = 0.4$ being here considered for the
142   porous medium.

143   Solute transport is then simulated across each conductivity field by a particle tracking approach
144   (Le Borgne et al., 2008). A number of 10^5 h particles (see (2)), which is selected to represent a full
145   pore volume (whose magnitude is evaluated through the initial condition, i.e., before porosity and
146   permeability are altered by the reactive processes) at constant pH = 3.5, is divided by the domain
147   length and multiplied by the mean velocity ($\hat{\boldsymbol{v}}$, as evaluated from (4) across the whole domain). A
148   total amount of particles evaluated as $Integer(10^5/L \cdot \Delta t \cdot \hat{\boldsymbol{v}})$ is then injected into the system at
149   regular time intervals ($\Delta t = 0.1$ min). Particles are injected at the very beginning of each time step Δt
150   and are flux-weighted according to the conductivity distribution at the inlet. The particles representing
151   a full pore volume correspond to $M_{H^+} = 10.79$ moles of H^+, the same amount being injected across
152   the simulation course to obtain a constant pH = 3.5 in the injected fluid, while absence of h particles
153   is taken to correspond to pH = 8. We then evaluate the pH value (or H^+ molar mass) associated with
154   each h particle by dividing the total number of H^+ moles required to obtain a pH = 3.5 (i.e., 10.79
155   mol of H^+) by the pore volume (as represented by 10^5 h particles).

156   The upper and lower boundaries of the domain are reflective while the outlet boundary is
157   absorbing. Particle migration is simulated through

158    $$\boldsymbol{d} = \boldsymbol{v}[\boldsymbol{x}(t_k)]\delta t + \boldsymbol{d}_D \tag{4}$$

159   where $\boldsymbol{d}$ is particle displacement, $\boldsymbol{x}(t_k)$ is the vector identifying spatial coordinates of particle location
160   at time t_k, $\boldsymbol{v}$ is fluid velocity at $\boldsymbol{x}(t_k)$, $\delta t = \delta s/v$ is the temporal displacement magnitude (v is the norm
161   of $\boldsymbol{v}$), and $\boldsymbol{d}_D$ is the diffusive displacement. The latter is evaluated as $\boldsymbol{d}_D = N[0,1]\sqrt{2D_m\delta t}$, where
162    $N[0,1]$ represents a two-dimensional vector of random variables, whose entries are mutually
163   independent and sampled from a Gaussian distribution with zero mean and unit variance, $D_m = 10^{-5}$
164   cm^2/min representing diffusion. The value of δs is selected to be an order of magnitude less than Δ,
165   to accurately sample the velocity variability within a conductivity block. It is noted that, while taking
166   into account pore-scale processes within a continuum-scale model through a local scale dispersion
167   could be a modeling option, this would add an additional level of complexity to our numerical
168   simulation without modifying the key elements of our work, which is focused on the interaction
169   between flow patterns and reactive processes. In this context, our modeling choice is to represent
170   macro-dispersive effects through averaging (in a multi-realization context) the effect of fluctuations

171 of velocity arising between diverse realizations of the conductivity field. Consistent with this, we rely
172 on a constant and isotropic diffusion coefficient that can be associated with an advection-dominated
173 transport regime (as quantified in terms of a Péclet number, as seen in the following). This choice is
174 also consistent with previous works (e.g., Aquino and Bolster, 2017; Wright et al., 2021).

175 Coupling between particle evolution and the geochemical setup illustrated in Section 2.1 is
176 achieved in two steps. First, we advance all particles according to the displacement mechanism
177 described above. Second, we satisfy the equilibrium condition (2) by equilibrating both co and h
178 within each cell, leading to precipitation or dissolution of a calcite mineral. The calcite volume to
179 mole ratio is taken as $M_{CaCO_3} = 37 \frac{cm^3}{mol}$ (Morse & Mackenzie, 1993) and the equilibrium between h
180 and co particles (according to (2)) leads to a local precipitation (or dissolution) of the solid. We update
181 in time the spatial distribution of porosity assuming that it is characterized by a uniform change within
182 each individual domain cell. We finally update conductivity through the Kozeny-Carman (KC)
183 formulation

184 $$k(ar)_{ij} = k(br)_{ij} \cdot \frac{\theta(ar)_{ij}^3}{\left(1-\theta(ar)_{ij}\right)^2} \cdot \frac{\left(1-\theta(br)_{ij}\right)^2}{\theta(br)_{ij}^3}; \qquad \theta(ar)_{ij} = \theta(br)_{ij}(1 \mp M_{CaCO_3} \cdot M_{H^+}) \qquad (5)$$

185 where $k(ar)_{ij}$ and $\theta(ar)_{ij}$ are conductivity and porosity, respectively, after the reaction (ar) has
186 taken place, while $k(br)_{ij}$ and $\theta(br)_{ij}$ are their counterparts before the reaction is observed,
187 subscripts i and j being identifiers of a given cell. The process is repeated for each particle in each of
188 the cells until an equilibrium between co and h is reached. We set an upper and a lower bound of 0.1
189 and 0.9, respectively, for porosity, to avoid the occurrence of unphysical porosity values. These
190 constraints are set for consistency with our assumptions, i.e., to consider Darcy flow across the porous
191 domain. A complete clogging (or opening) of a void space would require a different mathematical
192 and conceptual treatment, which is beyond the scope of our study. Precipitation is treated numerically
193 in a corresponding way.

194 We numerically calculate the updated local head and fluid velocity distributions from (4) at
195 time intervals of $10\,\Delta t$, to reduce constraints associated with computational costs. The computational
196 cost of each realization is between 1~3 days (depending on the value of σ_0^2), upon relying on a 16
197 Xeon 2.6 Ghz processor with 64 GB RAM. With reference to the sensitivity of the results to the
198 numerical parameters, we note that: (*a*) when considering single realizations, the results showed only
199 minute sensitivity to increasing the number of particles by a factor of 10 (less than 3% difference in
200 the results was observed); (*b*) results display a slightly larger sensitivity to the time step, otherwise
201 resulting in a difference of less than about 5% in the amount of reaction when decreasing the time
202 interval by an order of magnitude; and (*c*) preliminary analyses aimed at assessing possibe influences
203 of the grid size on the key results of the study imbued us with confidence about the quality of the
204 results obtained with the grid size employed in the study (details not shown), which we select as good
205 compromise between computational accuracy and execution time constraints, in light of our
206 objectives.

207 The updated conductivity field is extracted and stored at the above mentioned regular intervals
208 of $10\,\Delta t$. Transport of a non-reactive solute pulse is then simulated across each of these updated fields
209 to capture the temporal evolution of the key parameters driving effective transport (see Section 2.3).
210 While noting that natural porous media can exhibit complex relationships between permeability and
211 porosity (Luquot & Gouze, 2009), which may not always be interpreted through the KC model (6),
212 we employ the latter formulation because it is considered as a reference model in the literature and

can serve as a proxy for alternative improved parameterizations (Erol et al., 2017). We also recall that we consider local equilibrium, this choice being consistent with the specific objective of this work which is related to the characterization of transport under dynamic evolution of continuum-scale quantities such as conductivity, rather than being focused on a detailed characterization of the effects of the reactive process on the pore-scale structure (as reflected, e.g., by local changes of specific surface area).

2.3 Quantities of interest

The workflow described in Section 2.2 enables one to extract computationally-based quantities employed to characterize the analyzed reactive transport setup. As stated in Section 2.2, we simulate a tracer test within the original fields as well as within those modified by precipitation/dissolution. Particles are displaced through the action of advection and diffusion following a pulse (flux-weighted) injection at the inlet. These non-reactive transport simulations are performed to assess base values of parameters characterizing solute transport (*a*) prior to starting the reactive transport simulation as well as (*b*) at specific times after reaction changed the field. The empirical PDF of particle waiting times is assessed from the corresponding histogram starting by evaluating particle waiting times within a given domain cell through the inverse of the particle velocity computed at each time step multiplied by the cell length and weighted by the number of particles visiting the cell. This PDF is then used to estimate the parameters of the TPL model

$$\psi(t_w) = \frac{n}{t_1} \frac{\exp\left(-t/t_2\right)}{\left(1+\frac{t}{t_1}\right)^{1+\beta}} \tag{6}$$

where t_w is the waiting time of a particle within a given domain cell, t_1, t_2, and β are model calibration parameters, which are estimated through a standard least square technique. Note that previous results have shown that the parameters obtained from (6) can be readily used to interpret breakthrough curves associated with non-reactive solutes (Edery et al., 2014).

The velocity fields are examined upon computing the evolution of the velocity and conductivity fields statistics, as described in the following. Let us consider a discrete field of a generic quantity z_{ij} evaluated in a given cell ij. In the particle tracking numerical simulations we quantify $n_{ij}(t)$ as the number of particles that have visited cell ij along the simulation up to a given time t. Thus, we evaluate two relative frequency (or empirical probability) distributions, i.e., $f(z_{ij})$ and $f(nz_{ij})$, hereafter termed as unweighted and weighted distribution of the variable z_{ij}, respectively. We define the weighted variable $nz_{ij}(t) = n_{ij}(t)z_{ij}/\bar{n}(t)$, where $\bar{n}$ is the average value of n_{ij}. Note that the adopted weighting scheme corresponds to weighting z_{ij} by the solute mass distribution. Average values of the weighted and unweighted distributions (hereafter denoted as $\bar{z}$ and $\overline{nz}$, respectively) can then be evaluated. In the following we perform particle weighting in the non-reactive as well as in the reactive transport scenarios. Distribution weighting by reactive particles is indicated by n_R, meaning that weighting is performed based on the reactive transport simulations (i.e., considering h and co particles as explained above). The plain symbol n indicates weighting by non-reactive particles, employed to simulate conservative tracer tests as detailed above. The variable z_{ij} is taken to correspond to either the cell log-conductivity y_{ij} or fluid velocity v_{ij} in the results illustrated in Section 3.

3.Results

253   We start our analyses by simulating transport of a non-reactive tracer across the generated
254   heterogeneous conductivity domains. As log-conductivity variance increases, the range of
255   conductivity values naturally increases, this being reflected in the distribution $f(y_{ij})$ (see, e.g., Figure
256   1 a-c (blue circles)). The shape of weighted conductivity distributions, $f(ny_{ij})$, differs from the one
257   of $f(y_{ij})$, consistent with the observation that particles are chiefly channelled towards preferential
258   flow pathways. The latter distributions tend to be shifted towards high conductivity values and are
259   characterized by an enhanced mean conductivity value as compared against their generated
260   (unweighted) counterparts (see conductivity mean and weighted mean values in Table 1, and the
261   results corresponding to the blue and red circles depicted in Figure 1 a-c). This shift is imprinted onto
262   the probability density function (PDF) of the waiting times and onto its associated TPL parameters
263   (see Figure 2 a-c), consistent with prior studies (Edery et al., 2014; Edery, Geiger, et al., 2016; Edery,
264   2020). We then simulate reactive transport across the collection of generated fields, allowing for
265   precipitation (and/or dissolution) of calcite and assessing the evolution of the conductivity field
266   according to the Kozeny-Carman formulation introduced in Section 2. Conductivity, head, and
267   velocity fields, as well as particle visitations, $n_{ij}(t)$, associated with species h and co are sampled
268   across time.

269   After 200 Δt have elapsed (corresponding to a total simulation time of 20 min, i.e., a full pore
270   volume) a set of h particles connecting the inlet to the outlet of the system is clearly visible (see
271   Figure 3 a and b), these particles being non-uniformly distributed in space. Figure 3a and b depict a
272   heat map of the h particles distribution at time $t = 20$ min (i.e., corresponding to the first pore volume),
273   clearly evidencing the emergence of regions of preferential flow (PF). We also note that the number
274   of h particles density (corresponding to concentration) tends to decrease with increasing distance
275   from the inlet, these being replaced by co particles, consistent with the observation that they are
276   consumed during the course of the reactive process which induces dissolution of the host solid matrix.
277   The h and co particles attain equilibrium within cells away from the inlet. As such, reaction can only
278   take place if a particle leaves (or enters) a cell under the action of advection and/or diffusion leading
279   to a new equilibrium state. When examining the alteration of conductivities due to the
280   dissolution/precipitation reaction, we note that dissolution (corresponding to an increase of
281   permeability values) is primarily tied to the preferential flow pathways. Otherwise, precipitation is
282   seen to take place in regions close (on average) to these pathways. The highest strength of
283   precipitation is observed in the proximity of the preferential pathways, to then decrease with distance
284   from these.

285   Figures 3c and e depict the regions where conductivity has increased (due to dissolution) or
286   decreased (due to precipitation), respectively. The h particles invading the domain closely follow the
287   PFs displaying a fingering pattern, leading to a corresponding dissolution pattern associated with
288   locally increased conductivities. Since conductivity values along the PFs are typically higher (on
289   average), dissolution is increasing these conductivities even further, giving rise to a self-sustained
290   enhancing mechanism. The concentration of h particles reaches a local (i.e., within a given cell)
291   equilibrium with the produced co particles. Hence, dissolution will take place where transport induces
292   shifts in concentration that need to be compensated by the dissolution/precipitation process to
293   maintain local equilibrium. Such scenarios can be attained (*i*) by co particles exiting the preferential
294   flow pathways due to the action of diffusion (i.e., they leave locations where concentration of h
295   particles is large upon diffusing towards higher pH regions where they precipitate) or (*ii*) by h
296   particles traveling through the fast preferential paths and advancing through these. Figure 3g and h
297   display regions with dominating dissolution or precipitation for cells outside and within the PFs,

298 respectively. Here cells associated with PFs are identified upon relying on particle visitations
299 following Edery et al. (2014). Dissolution dominates within the PFs (as indicated by the red cells in
300 Figure 3h), because h particles are injected through a flux-weighted boundary condition. On the other
301 hand, the produced co particles do not precipitate at locations corresponding to the high h
302 concentration residing in the PFs. These may precipitate away from these regions, where they
303 experience low concentrations of h particles. Thus, we observe a reduction of conductivity taking
304 place in regions adjacent to the PFs (Figure 3b and g). In summary, our computational results
305 document an increase of conductivity along the preferential pathways jointly with a conductivity
306 reduction within regions close to these and along directions approximately normal to them.

307 Changes of conductivity values ensuing precipitation/dissolution are clearly visible by the
308 broadening of the unweighted log-conductivity distribution $f(y_{ij})$, see Figure 1d-f, and Figure 1g-i
309 (blue circles), evaluated at times $t = 10$ and $t = 20$ min, respectively. The reaction dynamics leads to
310 a conductivity field characterized by a slightly increased average value, given that our computational
311 analyses entail the injection of an acid fluid into the system (see Table 1 for details). Detailed
312 inspection of Figure 1d and f reveals that precipitation takes place across a slightly larger area than
313 dissolution, i.e. values of the frequency distribution $f(y_{ij})$ associated with low conductivities tend to
314 increase at a larger rate rather than those corresponding to high conductivities (the left tail of the
315 distributions becomes heavier than the right tail with the progress of reaction). The
316 weighted ($f(ny_{ij})$) and unweighted ($f(y_{ij})$) distributions (red and blue circles in Figure 1d-f, and
317 Figure 1g-i at time $t = 10$ and $t = 20$ min, respectively) are visibly broadening, being associated with
318 an average conductivity which is higher than the one of the originally generated conductivity domains
319 (see Table 1). As stated above, dissolution is focused along the preferential pathways, which comprise
320 an area of limited extent with respect to the whole field.

321 The above documented mechanism and its signature on the weighted and unweighted
322 conductivity frequency distributions are sensitive to the initial log-conductivity variance, σ_0^2. When
323 considering both distributions $f(y_{ij})$ and $f(ny_{ij})$, associated with the case $\sigma_0^2 = 1$, the distributions
324 variance are seen to increase in time, as compared to the values attained at the beginning of the
325 simulation (i.e., prior to reaction; see Figure 1a to d and g, and Table 1). Otherwise, as the initial
326 heterogeneity increases (see, e.g., $\sigma_0^2 = 3,5$) mean and variance associated with the weighted and
327 unweighted conductivity distributions display only minor changes (approximately 10%) across the
328 temporal window considered. The conductivity fields characterized by the lowest σ_0^2 value are
329 associated with preferential pathways that are not starkly recognizable when analyzed under non-
330 reactive transport conditions. These channels become more clearly distinguishable as reactions induce
331 an increase of the conductivities along the PFs. At the same time, precipitation causes a decrease of
332 the conductivity outside the PF. This leads to an increased importance of the left tail of $f(y_{ij})$,
333 corresponding to an increase of low conductivity values (see Figure 1, left middle and bottom rows).

334 With reference to the highest conductivity variance analyzed, the reaction patterns for the
335 precipitation and dissolution lead to a smaller relative change between conductivity frequency
336 distributions evaluated prior and after the reaction. Relative changes between the unweighted and
337 weighted conductivity frequency distributions (including the ensuing mean and variance listed in
338 Table 1) evaluated before and after the reaction are less pronounced as the variance of the generated
339 conductivity field increases (see Figure 1 middle and right columns and Table 1). This is related to
340 the observation that, as log-conductivity variance increases, preferential pathways in the originally
341 generated field become markedly more distinct. Thus, relative differences between unweighted and
342 weighted conductivity histograms are seen to diminish in time because the flow field is already

8

343 organized according to well-identified pathways and tends to preserve its initial pattern (Figure 1d-f,
344 and Figure 1g-i at time $t = 10$ and $t = 20$ min, respectively). Note that low order statistics (i.e., mean
345 and variance) of velocity and conductivity display only a minute evolution with the progress of
346 reaction, in spite of the relevant changes exhibited by the tails of the frequency distributions (see
347 Figure 1) for all considered values of σ_0^2, the latter feature being relevant when addressing non-
348 Fickian transport, as further discussed below.

349 As stated in Section 2.2, the conductivity fields altered through precipitation/dissolution and
350 extracted at regular time intervals of $10 \, \Delta t$ are subject to non-reactive transport analyses and the
351 ensuing evolution of the parameters of the TPL model (6) is analyzed. Key results of these analyses
352 are listed in Table 1 with reference to the original (unaltered) conductivity fields and at the final
353 simulation time (i.e., at time $t = 200 \, \Delta t$). Analysis of the results associated with transport across the
354 log-conductivity field characterized by the smallest original variance (i.e., $\sigma_0^2 = 1$) and listed in Table
355 1 indicates that the changes of the sample log-conductivity PDF induced by the progress of the
356 reaction are reflected by the parameters of the TPL model (6). These transition from estimated values
357 corresponding to an effective Fickian transport regime (corresponding to $\beta = 2$, see also Figure 2a)
358 to values denoting a highly non-Fickian effective transport setting, manifested by the widening of the
359 support of the waiting time PDF $\psi(t_w)$ (see also Figure 2d and 2g, for results obtained at $t = 10$ and
360 20 min, respectively). Effective transport in the domain with the highest variance (i.e., $\sigma_0^2 = 5$; see
361 Table 1) is characterized by estimated TPL parameters corresponding to a non-Fickian signature also
362 prior to the occurrence of precipitation/dissolution (Figure 2c). Such a signature is then further
363 enhanced after reaction has altered the conductivity field, yet displaying a less marked evolution of
364 the shape of the $\psi(t_w)$ as compared to the case $\sigma_0^2 = 1$ (see also Figure 2f and i for $t = 10$ and 20 min,
365 respectively).

366 The observed temporal changes in conductivity and the ensuing local dynamics of transport
367 pattern yield global variations in the reaction rate. Consistent with prior studies and the imposed
368 boundary conditions, the mean velocity associated with the originally generated conductivity domains
369 increases with σ_0^2. As the reaction progresses and the conductivity fields change, the increased area
370 subject to dissolution leads to a slight increase of the mean velocity for all of the σ_0^2 analyzed. To
371 analyze the influence of the preferential flow on the velocity that is affecting particle transport, we
372 consider the average value $\overline{n_R v}$, evaluated upon considering weighting by the number of reactive
373 particles, n_R, visiting each cell (where the term reactive particles denotes both h and co particles
374 employed in the context of the reactive transport simulations). The weighted average velocity displays
375 an initial increase over time due to the increase of conductivity within the preferential pathways.
376 When considering the relative change across the whole simulation time, values of the temporal
377 increase of $\overline{n_R v}$ are similar across the three heterogeneity levels examined, i.e., they are seemingly
378 independent of σ_0^2. However, results in Figure 4a also reveal that the average velocity $\overline{n_R v}$ displays
379 distinct temporal histories depending on σ_0^2. In particular, the value of $\overline{n_R v}$ tends to attain an
380 asymptotic value at time $t \approx 7$ min for $\sigma_0^2 = 5$, while showing a sustained increasing trend for $\sigma_0^2 =$
381 1. This result suggests that the feedback between reaction and flow patterns reaches an asymptotic
382 condition faster in systems characterized by higher heterogeneity.

383 The temporal evolution of the velocity fields due to the precipitation/dissolution reaction and
384 the resulting conductivity changes lead to time-dependent reaction pattern and reaction rates. The
385 Damköhler number is infinite on a local scale in our computational analyses, because the reaction is
386 instantaneous. When considering the entire system, transport processes induce a net overall reaction
387 rate that can be quantified as the sum of the total conductivity changes across time

9

388     $(Sum(|\Delta k_{ij}|) \, [\frac{cm}{sec}])$. The latter incorporates both positive and negative changes of hydraulic
389   conductivity and therefore quantifies the overall intensity of precipitation and dissolution processes
390   in the domain. The quantity $Sum(|\Delta k_{ij}|)$ is evaluated across all realizations for each of the σ_0^2 values
391   considered and is depicted in Figure 4b as a function of time. These results indicate that the overall
392   reaction rate increases in time with a similar rate for all considered values of σ_0^2 (figure 4b) at early
393   times. The observed increase is consistent with the initially advancing of the reaction front across the
394   domain. We observe that the reactive processes magnitude is proportional to σ_0^2. For low initial levels
395   of heterogeneity, conductivity values along the preferential pathways are closer to the average field
396   conductivity than what can be observed for the highly heterogeneous domains. As such, the portion
397   of the domain where precipitation or dissolution can take place increases at a rate proportional to σ_0^2.
398   As the reaction front reaches the domain outlet, the dissolving front found in the PF leaves the domain.
399   Hence, the global variation in conductivity (which is proportional to the magnitude of reactive
400   processes) tends towards an asymptotic value, corresponding to the diffusion-controlled solute
401   exchange along a direction transverse to the preferential pathways (see Figure 3). In agreement with
402   results shown in Figure 4a, this transition towards an asymptotic regime takes place earlier for larger
403   values of σ_0^2, while a smaller initial heterogeneity implies a longer transient period.

404   **4.Conclusions**

405 Our computational study tackles the quantitative characterization of the feedbacks between
406 precipitation and dissolution reaction dynamics taking place in randomly heterogenous conductivity
407 fields associated with various degrees of spatial heterogeneity. Our work leads to the following key
408 conclusions.

409   •   Joint occurrence of precipitation and dissolution is tightly coupled with the existence of
410   preferential flow pathways. Conductivity increase due to the dissolution reaction along such
411   paths leads to enhance particle migration along these. The dominance of preexisting
412   preferential flow regions on the (reactive) transport pattern across the field is therefore further
413   reenforced and self-sustained across time. At the same time, diffusion promotes displacement
414   of particles, leading to precipitation (and hence a progressive reduction over time of local
415   conductivities) at locations in the proximity of these.
416   •   Reactive processes yield an increase over time of the range of conductivity values across the
417   domain, eventually leading to a widening of the support of solute waiting times and
418   conductivity distributions. The clear separation between regions where dissolution or
419   precipitation takes place is reflected in sample distributions of conductivity which tend to
420   become visibly left skewed with time, a feature which is associated with precipitation taking
421   place in low conductivity cells located in the proximity of existing preferential flow
422   pathways.
423   •   Solute mass weighted conductivity and velocity distributions are at the basis of our
424   characterization of the parameters of a TPL model which is at the core of the characterization
425   of the probability density function of particle travel/waiting times and enables us to capture
426   effective (upscaled) non-Fickian transport behaviors. With the progress of
427   precipitation/dissolution reactions, transport shifts towards an increasingly acute non-Fickian
428   effective behavior (see Figure 2 and ensuing parameter values listed in Table 1). The latter is
429   then seen as a direct outcome of the documented feedbacks between transport and reactions
430   taking place in heterogeneous porous media. The evolution of TPL model parameters towards
431   a pronounced non-Fickian behavior is associated with only minor changes of the mean and
432   variance of log-conductivity values. This result is consistent with the conceptual picture that

the tails of flux and hydraulic conductivity distributions carry critical information to characterize transport while displaying only a minor effect on low order statistics associated with these quantities. Our results suggest that this feature must be acknowledged to properly characterize transport in the presence of precipitation/dissolution. In this context, we recall that our study is not aimed at exploring the skill of any specific transport model to interpret non-reactive transport across the conductivity fields prior and/or after reaction takes place, this particular analysis being deferred to a future study.

- We observe the emergence of an asymptotic regime in highly heterogeneous systems, where the (averaged) solute velocity attains a constant value even in the presence of reaction. This suggests the occurrence of an equilibrium state between reactive processes and transport under the flow conditions analyzed. This regime is attained because the effects of locally occurring precipitation and dissolution balance each other at the overall scale of the system, so that the ensuing (ensemble-averaged) solute velocity remains unaffected. The time required to attain such an asymptotic state increases with decreasing initial heterogeneity of the conductivity field, thus suggesting that pre-asymptotic behaviors may be more relevant in initially (i.e., prior to reaction taking place) homogeneous systems.

Our results are based on numerical simulations and may be used to inform upscaling approaches to capture the pre-asymptotic and asymptotic dynamics of reactive transport in heterogeneous systems through simplified models. Future computational studies might also include an assessment of the importance of initial/boundary conditions and/or of solute injection mode on the emergence of non-Fickian transport features, with special emphasis on locations close to the inlet boundary which might then have an impact on the overall solute residence times and related statistics.

	$\sigma_0^2 = 1$			$\sigma_0^2 = 3$			$\sigma_0^2 = 5$		
t [min]	0	10	20	0	10	20	0	10	20
$\bar{y}$	0.15	0.16	0.17	0.45	0.46	0.46	0.66	0.67	0.69
$\overline{ny}$	0.32	0.33	0.35	0.83	0.84	0.86	1.20	1.19	1.21
$\sigma^2(y_{ij})$	0.97	1.20	1.37	2.80	3.10	3.26	4.60	4.96	5.11
$\sigma^2(ny_{ij})$	0.99	1.21	1.41	2.80	3.07	3.21	4.60	4.85	5.00
$\overline{v_T}$	0.36	0.37	0.38	0.41	0.42	0.43	0.45	0.46	0.47
$\overline{nv_T}$	0.45	0.47	0.50	0.67	0.70	0.72	0.86	0.88	0.90
β	2.00	1.40	1.05	1.70	1.20	0.95	1.40	0.80	0.60
t_1	0.10	0.09	0.06	0.10	0.07	0.03	0.08	0.03	0.01
$\mathrm{Log}_{10}(t_2)$	1.0	2.5	2.8	1.5	2.2	2.9	1.6	2.5	3.0

Table 1. Values of mean and variance of unweighted and weighted log-conductivity distributions and estimated parameters of the effected TPL model obtained through calibration of (6) against the computed distributions of particle waiting times in the domain cells. Results are listed for the three values of the initial log-conductivity variance (σ_0^2) and are obtained from non-reactive transport simulations performed across conductivity fields resulting from reactive transport simulations at selected times.

462
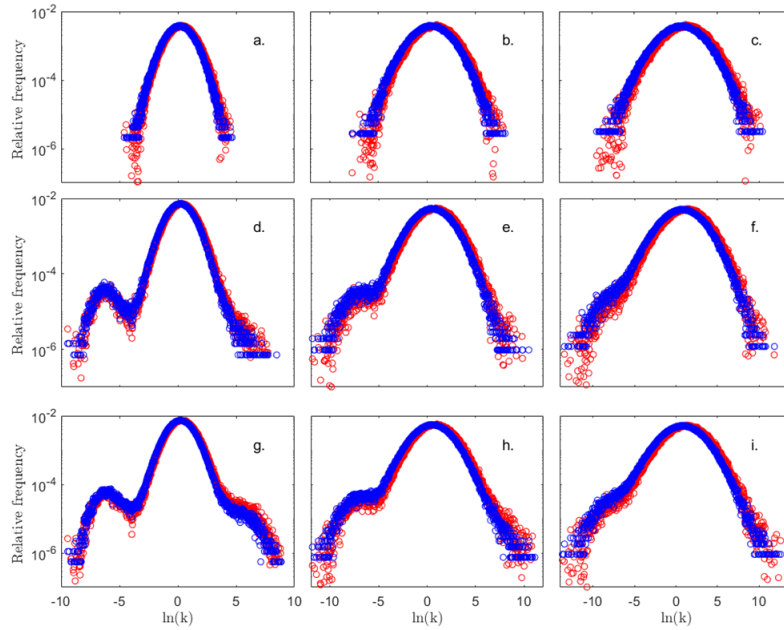
Figure 1. Relative frequency distributions $f(y_{ij})$ (blue circles) and $f(ny_{ij})$ (red circles) for a tracer test performed on the conductivty field prior to reaction and those associated with reactive simulation times of 10 and 20 minutes. Results correspond to $\sigma_0^2 = 1,3,5$ (left, middle and right columns, respectively) and to $t = $ (a-c) 0, (d-f) 10, and (g-i) 20 min. Mean and variance of these distributions are listed in Table 1.

467
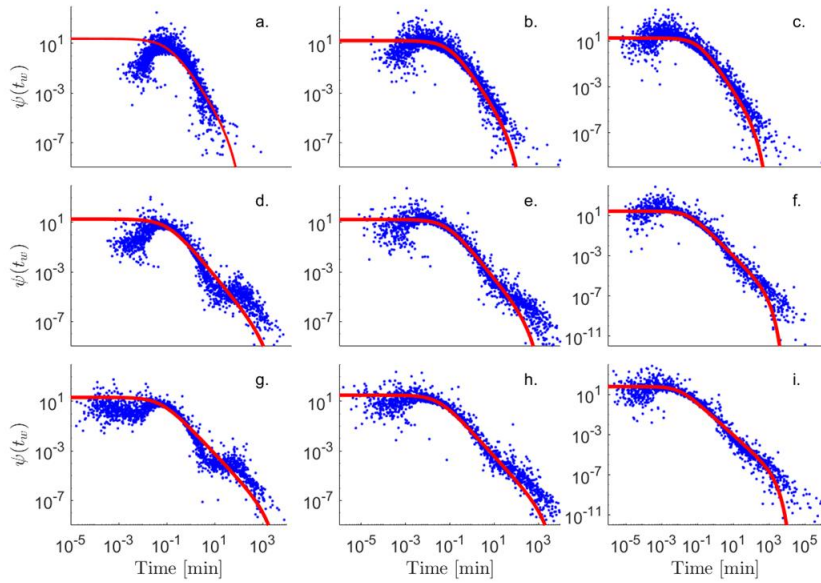
468
469 Figure 2. Sample and modeled probability density function $\psi(t_w)$ of particle waiting times for a tracer test performed on the conductivty field prior to reaction those associated with reactive simulation times of 10 and 20 minutes. Results correspond to $\sigma_0^2 = 1,3,5$ (left, middle and right columns, respectively) and $t = $ (a-c) 0, (d-f) 10 min, and (g-i) 20 min. Values of TPL parameters estimated by calibrating model (6) on the sample distributions are listed in Table 1.

12

473
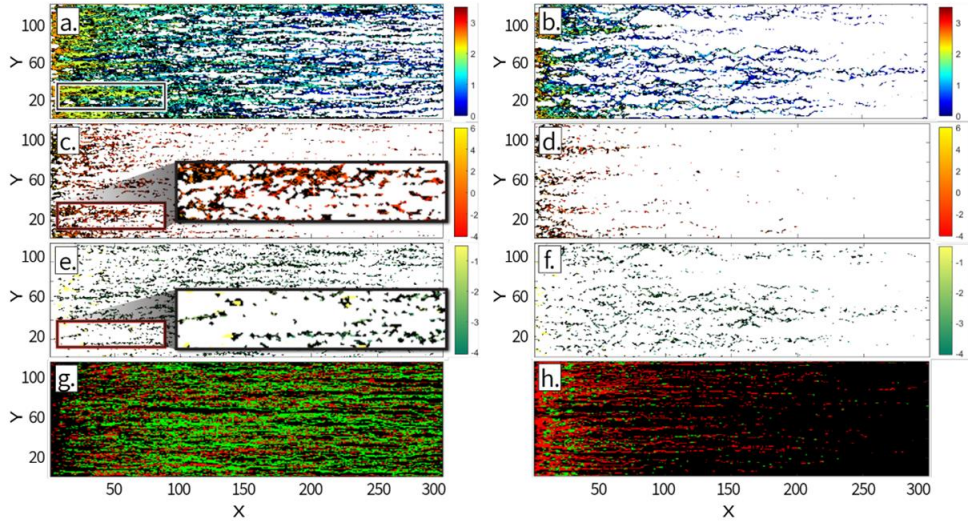

474
475 *Figure 3. Heat map representing (a,b) $Log_{10}(n_{Rij})$, i.e., the number of h particles visiting each cell for $\sigma_0^2 = 1$ and 5, respectively,*
476 *and (c-f) relative change in hydraulic conductivity at time t = 20 min (corresponding to the first pore volume) with respect to the*
477 *initially generated values for $\sigma_0^2 = 1$ (c and e) and $\sigma_0^2 = 5$ (d and f). Panels c and d display positive changes in conductivity with*
478 *respect to the initial field, while panels e and f display negative changes in conductivity, both positive and negative changes being*
479 *represented in log-scale. Results correspond to a selected realizaton of the the log-conductivity fields. The highlighted box*
480 *illustrates the separation between regions where precipitation or dissolution take place. Panels g and h display cells associated with*
481 *a net decrease (green) and increase (red) of conductivity for cells outside (g) or within the PF (h), for $\sigma_0^2 = 1$.*

482

483
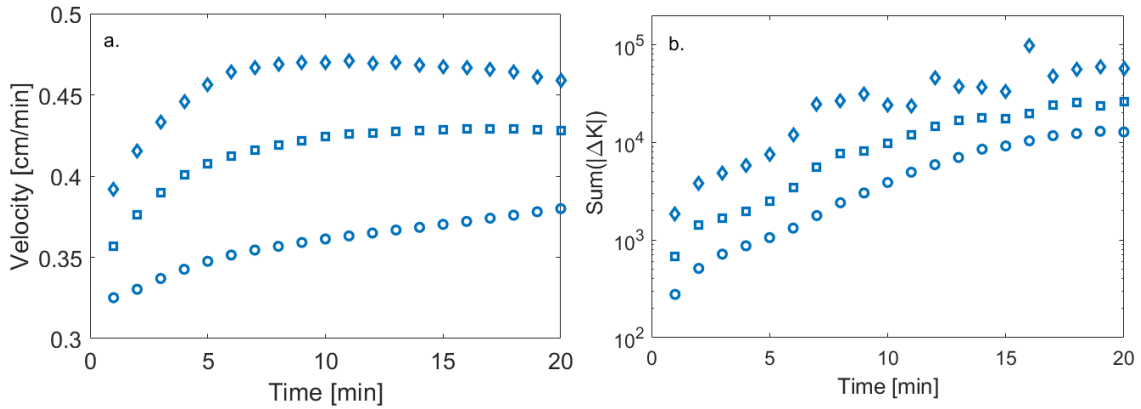
484 *Figure 4. Temporal evolution of (a) the weighted mean velocity $\overline{n_R v}$ (open symbols) and (b) the sum of all conductivity changes over*
485 *1 minut . Results correspond to $\sigma_0^2 = 1$ (circles), 3 (squares), and 5 (diamond).*

486

Acknowledgments

490

491 **References**

Ababou, R., McLaughlin, D., Gelhar, LynnW., & Tompson, AndrewF. B. (1989). Numerical simulation of three-dimensional saturated flow in randomly heterogeneous porous media. *Transport in Porous Media*, *4*(6). https://doi.org/10.1007/BF00223627

Atchley, A. L., Navarre-Sitchler, A. K., & Maxwell, R. M. (2014). The effects of physical and geochemical heterogeneities on hydro-geochemical transport and effective reaction rates. *Journal of Contaminant Hydrology*, *165*, 53-64. https://doi.org/10.1016/j.jconhyd.2014.07.008.

Aquino, T., & Bolster, D. (2017). Localized point mixing rate potential in heterogeneous velocity fields. *Transport in Porous Media*, 119, 391-402. https://doi.org/10.1007/s11242-017-0887-z.

Berkowitz, B., Cortis, A., Dentz, M., & Scher, H. (2006). Modeling non-Fickian transport in geological formations as a continuous time random walk. *Reviews of Geophysics*, *44*(2), RG2003. https://doi.org/10.1029/2005RG000178

Berkowitz, B., Dror, I., Hansen, S. K., & Scher, H. (2016). Measurements and models of reactive transport in geological media. *Reviews of Geophysics*, *54*(4), 930–986. https://doi.org/10.1002/2016RG000524

Cabeza, Y., Hidalgo, J. J., & Carrera, J. (2020). Competition Is the Underlying Mechanism Controlling Viscous Fingering and Wormhole Growth. *Geophysical Research Letters*, *47*(3). https://doi.org/10.1029/2019GL084795

Ceriotti, G., Guadagnini, L., Porta, G., & Guadagnini, A. (2018). Local and Global Sensitivity Analysis of *Cr (VI)* Geogenic Leakage Under Uncertain Environmental Conditions. *Water Resources Research*, *54*(8), 5785–5802. https://doi.org/10.1029/2018WR022857

Dalla Libera, N., Pedretti, D., Tateo, F., Mason, L., Piccinini, L., & Fabbri, P. (2020). Conceptual Model of Arsenic Mobility in the Shallow Alluvial Aquifers Near Venice (Italy) Elucidated Through Machine Learning and Geochemical Modeling. *Water Resources Research*, *56*(9). https://doi.org/10.1029/2019WR026234

Dentz, M., Gouze, P., & Carrera, J. (2011). Effective non-local reaction kinetics for transport in physically and chemically heterogeneous media. *Journal of Contaminant Hydrology*, *120–121*, 222–236. https://doi.org/10.1016/j.jconhyd.2010.06.002.

Dreybrodt, W., Lauckner, J., Zaihua, L., Svensson, U., & Buhmann, B. (1996). The kinetics of the reaction $CO_2 + H_2O \rightarrow H^+ + HCO_3^-$ as one of the rate limiting steps for the dissolution of calcite in the system H_2O-CO_2-$CaCO_3$. *Geochimica et Cosmochimica Acta*, 60(18), 3375-3381. https://doi.org/10.1016/0016-7037(96)00181-0.

Edery, Y. (2020). The topological origin of anomalous transport: Persistence of {\beta} in the face of varying correlation length. *ArXiv:1906.07061 [Physics]*. Retrieved from http://arxiv.org/abs/1906.07061

Edery, Y., Scher, H., & Berkowitz, B. (2011). Dissolution and precipitation dynamics during dedolomitization. *Water Resources Research*, *47*(8). https://doi.org/10.1029/2011WR010551

Edery, Y., Guadagnini, A., Scher, H., & Berkowitz, B. (2014). Origins of anomalous transport in heterogeneous media: Structural and dynamic controls. *Water Resources Research*, *50*(2), 1490–1505. https://doi.org/10.1002/2013WR015111

Edery, Y., Porta, G. M., Guadagnini, A., Scher, H., & Berkowitz, B. (2016). Characterization of Bimolecular Reactive Transport in Heterogeneous Porous Media. *Transport in Porous Media*, *115*(2), 291–310. https://doi.org/10.1007/s11242-016-0684-0

Edery, Y., Geiger, S., & Berkowitz, B. (2016). Structural controls on anomalous transport in fractured porous rock. *Water Resources Research*, *52*(7), 5634-5643. https://doi.org/10.1002/2016WR018942

Erol, S., Fowler, S. J., Harcouët-Menou, V., & Laenen, B. (2017). An Analytical Model of Porosity–Permeability for Porous and Fractured Media. *Transport in Porous Media*, *120*(2), 327–358. https://doi.org/10.1007/s11242-017-0923-z

Garing, C., Gouze, P., Kassab, M., Riva, M., & Guadagnini, A. (2015). Anti-correlated Porosity–Permeability Changes During the Dissolution of Carbonate Rocks: Experimental Evidences and Modeling. *Transport in Porous Media*, *107*(2), 595-621. https://doi.org/10.1007/s11242-015-0456-2

Golfier, F., Zarcone, C., Bazin, B., Lenormand, R., Lasseux, D., & Quintard, M. (2002). On the ability of a Darcy-scale model to capture wormhole formation during the dissolution of a porous medium. *Journal of Fluid Mechanics*, *457*, 213-254. https://doi.org/10.1017/S0022112002007735

Gómez-Hernández, J. J., & Journel, A. G. (1993). Joint Sequential Simulation of MultiGaussian Fields. In A. Soares (Ed.), *Geostatistics Tróia '92* (Vol. 5, pp. 85–94). Dordrecht: Springer Netherlands. https://doi.org/10.1007/978-94-011-1739-5_8

Krauskopf, K. B., & Bird, D. K. (1967). *Introduction to geochemistry* (Internat.3Rev.ed).

Le Borgne, T., Dentz, M., & Carrera, J. (2008). Lagrangian Statistical Model for Transport in Highly Heterogeneous Velocity Fields. *Physical Review Letters*, *101*(9), 090601. https://doi.org/10.1103/PhysRevLett.101.090601

Lichtner, P. (1988). The quasi-stationary state approximation to coupled mass transport and fluid-rock interaction in a porous medium. *Geochimica et Cosmochimica Acta*, 52, 143-165. https://doi.org/10.1016/0016-7037(88)90063-4.

Liu, P., Yao, J., Couples, G. D., Ma, J., & Iliev, O. (2017). 3-D Modelling and Experimental Comparison of Reactive Flow in Carbonates under Radial Flow Conditions. *Scientific Reports*, *7*(1), 17711. https://doi.org/10.1038/s41598-017-18095-2

Menke, H. P., Reynolds, C. A., Andrew, M. G., Pereira Nunes, J. P., Bijeljic, B., & Blunt, M. J. (2018). 4D multi-scale imaging of reactive flow in carbonates: Assessing the impact of heterogeneity on dissolution regimes using streamlines at multiple length scales. *Chemical Geology*, *481*, 27–37. https://doi.org/10.1016/j.chemgeo.2018.01.016

Morse, J. W., & Mackenzie, F. T. (1993). Geochemical constraints on $CaCO_3$ transport in subsurface sedimentary environments. *Chemical Geology*, *105*(1–3), 181–196. https://doi.org/10.1016/0009-2541(93)90125-3

Muljadi, B. P., Bijeljic, B., Blunt, M. J., Colbourne, A., Sederman, A. J., Mantle, M. D., & Gladden, L. F. (2018). Modelling and upscaling of transport in carbonates during dissolution: Validation and calibration with NMR experiments. *Journal of Contaminant Hydrology*, *212*, 85–95. https://doi.org/10.1016/j.jconhyd.2017.08.008

Noiriel, C., & Daval, D. (2017). Pore-Scale Geochemical Reactivity Associated with CO_2 Storage: New Frontiers at the Fluid–Solid Interface. *Accounts of Chemical Research*, *50*(4), 759–768. https://doi.org/10.1021/acs.accounts.7b00019

Rege, S. D., & Fogler, H. S. (1989). Competition among flow, dissolution, and precipitation in porous media. *AIChE Journal*, *35*(7), 1177–1185. https://doi.org/10.1002/aic.690350713

Riva, M., Guadagnini, A., Neuman, S. P., Janetti, E. B., & Malama, B. (2009). Inverse analysis of stochastic moment equations for transient flow in randomly heterogeneous media. *Advances in Water Resources*, *32*(10), 1495–1507. https://doi.org/10.1016/j.advwatres.2009.07.003

Saripalli, K. P., Meyer, P. D., Bacon, D. H., & Freedman, V. L. (2001). Changes in Hydrologic Properties of Aquifer Media Due to Chemical Reactions: A Review. *Critical Reviews in Environmental Science and Technology*, *31*(4), 311–349. https://doi.org/10.1080/20016491089244

582   Singurindy, O., & Berkowitz, B. (2004). Dedolomitization and flow in fractures. *Geophysical*
583   *Research Letters*, *31*(24), L24501. https://doi.org/10.1029/2004GL021594.

584   Wright, E. E., Sund, N. L., Richter, D. H., Porta, G. M., & Bolster, D. (2021). Upscaling
585   bimolecular reactive transport in highly heterogeneous porous media with the LAgrangian
586   Transport Eulerian Reaction Spatial (LATERS) Markov model. *Stochastic Environmental Research*
587   *and Risk Assessment*, 35, 15-29-1547. https://doi.org/10.1007/s00477-021-02006-z.

588